

Core formation and magma ocean outgassing set planetary N-S-C ratios

Colin Jackson (✉ cjackson2@tulane.edu)

Tulane University

Elizabeth Cottrell

Smithsonian Institution, National Museum of Natural History <https://orcid.org/0000-0002-9402-9394>

Zhixue Du

Guangzhou Institute of Geochemistry, Chinese Academy of Sciences <https://orcid.org/0000-0002-7716-2994>

Neil Bennett

California State University

Yingwei Fei

Carnegie Institution for Science

Article

Keywords: Core formation, magma

Posted Date: July 15th, 2020

DOI: <https://doi.org/10.21203/rs.3.rs-40405/v1>

License:   This work is licensed under a Creative Commons Attribution 4.0 International License.

[Read Full License](#)

1 **Title**

2 Core formation and magma ocean outgassing set planetary N-S-C ratios

3

4 **Authors**

5 Colin Jackson^{1*}, Elizabeth Cottrell², Zhixue Du³, Neil Bennett⁴, Yingwei Fei⁵

6 ¹ Department of Earth and Environmental Sciences, Tulane University, cjackson2@tulane.edu

7

8 ² Department of Minerals Sciences, Smithsonian Institution

9

10 ³ Guangzhou Institute of Geochemistry

11 ⁴ Department of Chemistry and Biochemistry, California State University, East Bay

12

13 ⁵ Carnegie Institution for Science

14 **Abstract**

15 Earth's volatile elements cannot be accounted for as mixtures of different chondrites, despite
16 their clear chondritic heritage. Early-acting, but as yet unidentified, processes apparently fractionated
17 volatile elements now contained by planets. Here we test the hypothesis that planetary-scale
18 differentiation, namely core formation and primordial atmosphere degassing, set Earth's distribution of
19 N, S, and C. To this end, we report new metal-silicate partitioning experiments on N up to 26 GPa and
20 3400 K; the highest pressure and temperatures conditions yet explored. Our results highlight a strong,
21 positive effect of pressure on nitrogen partitioning into cores. We apply our new experiments with
22 literature data for S and C partitioning to a model that couples core formation with degassing into the
23 primordial atmosphere, to demonstrate that volatile elements ratios for Earth, and potentially Mars and
24 Venus, can be set by primordial differentiation under conditions that also satisfy their moderately
25 siderophile element budgets.

26

27

28

29

30

31

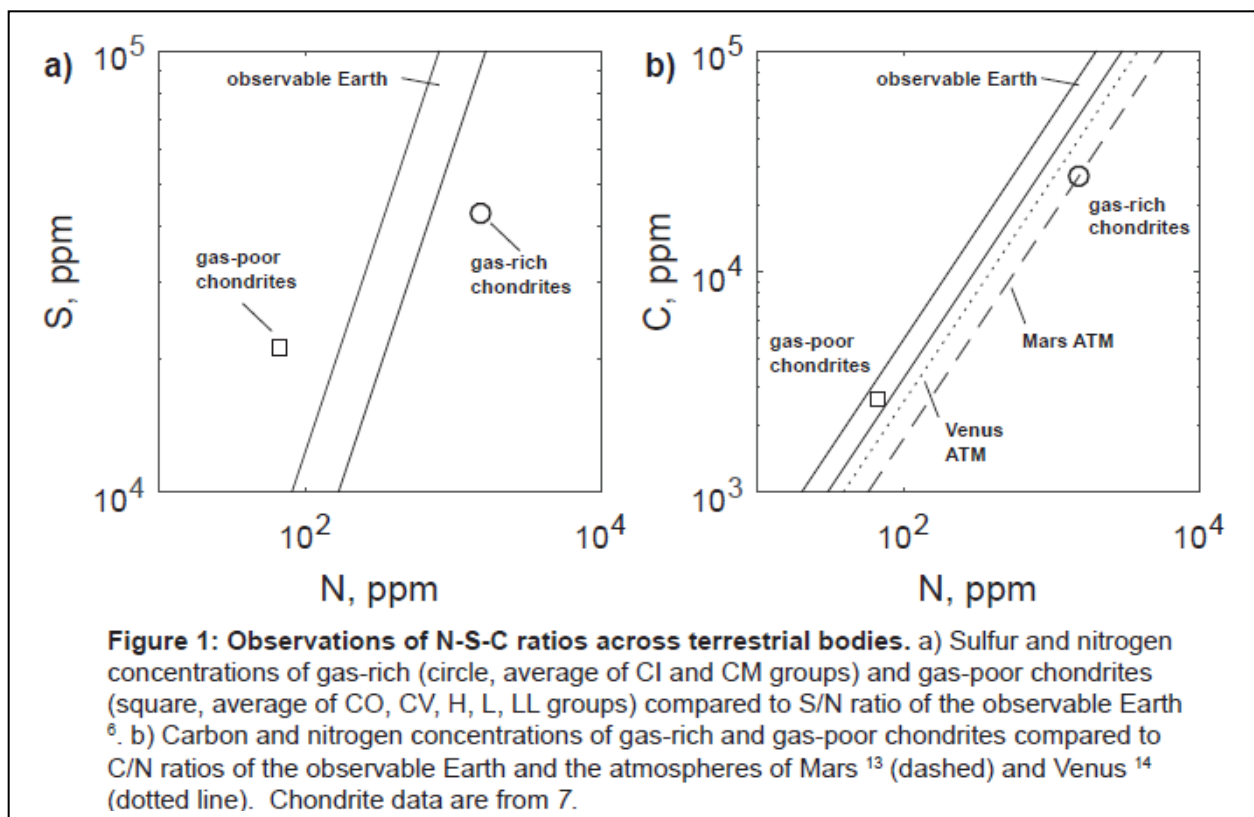
32

33

34

35 **Introduction**

36 Earth's highly volatile and life-essential elements, including nitrogen, sulfur, hydrogen, and
37 carbon, are isotopically linked to chondrites¹⁻³. Despite this isotopic heritage, the relative abundances of
38 life-essential elements observed within Earth and its atmosphere are not simple mixtures of different
39 chondritic components (Figure 1)⁴⁻⁶. Perhaps the most conspicuous observation here is that Earth
40 appears depleted in N relative to all other highly volatile elements, as indicated by elevated $(S/N)_{OE}$ and
41 $(C/N)_{OE}$ ratios (OE denotes the observable Earth, or the sum of the atmosphere, oceans, crust and
42 mantle) relative to gas-rich chondrites. This depletion, along with the less fractionated ratios associated
43 with S and C are fundamental expressions of the integrated processes that ultimately determine the
44 volatile budget of planets.



45 The explanation for N depletion has focused on the processes external to planets. The high
46 volatility of N⁸ raises the possibility that atmospheric loss in response to impacts of varying size
47 efficiently removed N, and potentially other volatile elements, from growing proto-planetary bodies^{9,10}

48 that ultimately comprise Earth. Similarly, gas-phase chemical reactions beyond the snow-line of the
49 proto-planetary disk may also lead to element fractionations¹¹. Ices and refractory C produced in this
50 environment can combine to create volatile-rich materials that are relatively N-poor. Radial mixing can
51 then introduce this N-depleted chemical signature into the inner solar system^{e.g., 12}.

52 A key corollary, when invoking processes external to planets, is that N depletion should be
53 systematic across the inner Solar System. In this case, the dominant role of exogenous processes in
54 determining the N depletions of planets may then extend to volatiles in general. However, Mars and
55 Venus do not appear as depleted in N as Earth is, at least according to their gas-rich chondrite-like
56 atmospheric C/N ratios^{13,14} (dashed and dotted lines in Figure 1b). Nitrogen isotopes for Mars further
57 indicate massive N loss from the atmosphere¹⁵, which may indicate Mars's mantle is enriched in N. This
58 all combines to suggest that Earth's N depletion is not a signature common to inner Solar System planets
59 (Figure 1a). Note that we do not consider H in our analysis because its behavior during accretion
60 remains highly uncertain^{c.f., 16,17}.

61 Accepting that exogenous processes are not solely responsible for the variety of N-S-C ratios
62 observed for the inner planets of the Solar System leads us to consider endogenous processes. The
63 formation of a metallic core is one such process thought to affect all inner Solar System planets, as well
64 as the differentiated planetesimals they formed from. Core formation fractionates elements on the basis
65 of their preference for the metallic phase. For the relatively low pressure and temperature (P - T)
66 conditions associated with core formation in planetesimals, sulfur and carbon both display a greater
67 preference for the metal phase (more siderophile behavior) than nitrogen^{e.g., 18-26}, provided planetesimal
68 S and C concentrations remain at levels associated with planets²⁷. Strongly siderophile S and C would
69 lead to low S/N and C/N observable ratios for planetesimals, the opposite of what is observed for Earth
70^{2,5,6}. This suggests that the chemical signature of low P - T core formation possessed by planetesimals was
71 subsequently overprinted during terrestrial accretion.

72 Such redistribution of elements during Earth’s accretion is expected on the basis of moderately
73 siderophile elements, such as Ni and Co, that have been used to argue for metal-silicate equilibrium at
74 extreme conditions (average pressures of 30 – 59 GPa^{28,29}). Accordingly, metal-silicate partitioning data
75 for N, S, and C collected at similar conditions are required to assess the role of core formation in
76 modulating Earth’s volatile element budget.

77 Here, we present new N partitioning data collected under the most extreme *P-T* conditions yet
78 explored and close to those thought to accompany Earth’s core formation. Combined with recently
79 reported metal-silicate partitioning data for S and C³⁰⁻³³, we demonstrate that $(S/N)_{OE}$ and $(S/C)_{OE}$ ratios
80 could be an inherent consequence of the deep differentiation process that is also required to explain the
81 abundances refractory elements in Earth’s mantle^{27,28}.

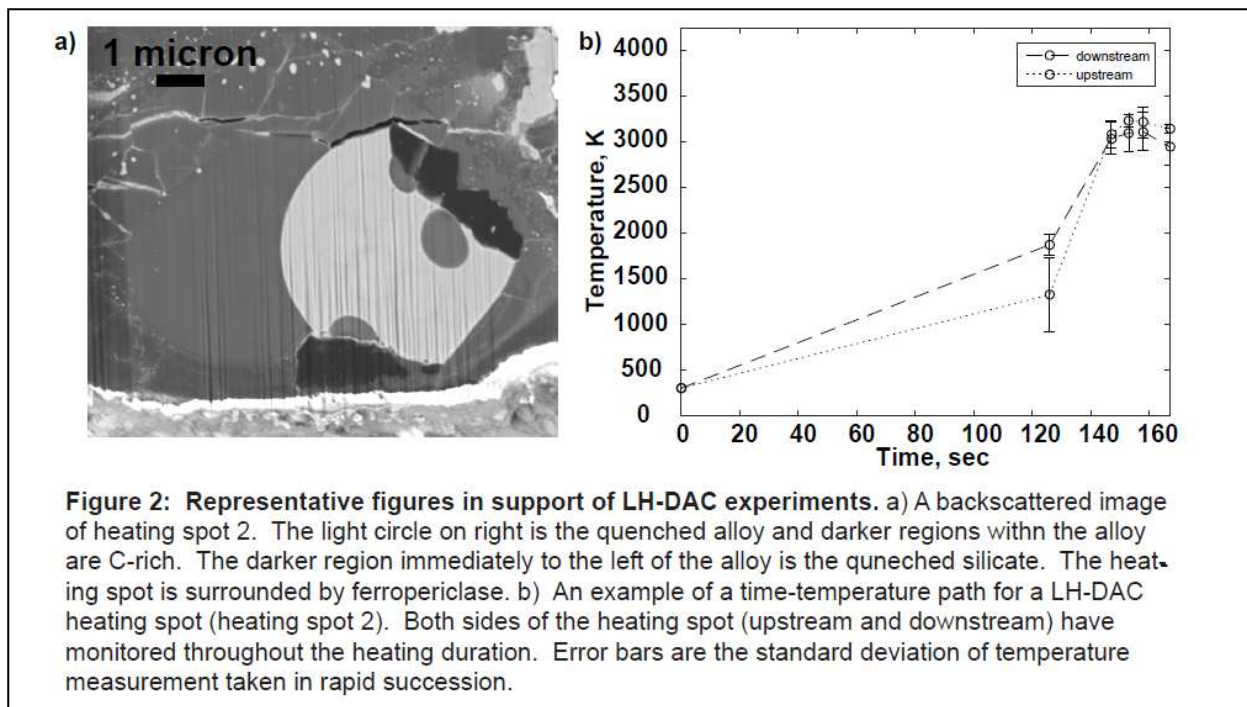
82 **Results**

83 **High *P-T* metal-silicate partitioning experiments for nitrogen**

84 We conducted N partitioning experiments between liquid metal (core) and liquid silicate
85 (magma ocean) between 1873-3437 K and 1-26 GPa. We employed both a piston cylinder device and
86 laser-heated diamond anvil cells (LH-DAC). Experimental fO_2 conditions ranged from IW-6.6 to IW-1.0,
87 (log unit deviations from iron-wüstite buffer). These experiments range up to the *P-T-X* conditions that
88 are directly relevant to the average core formation within Earth^{28,29}.

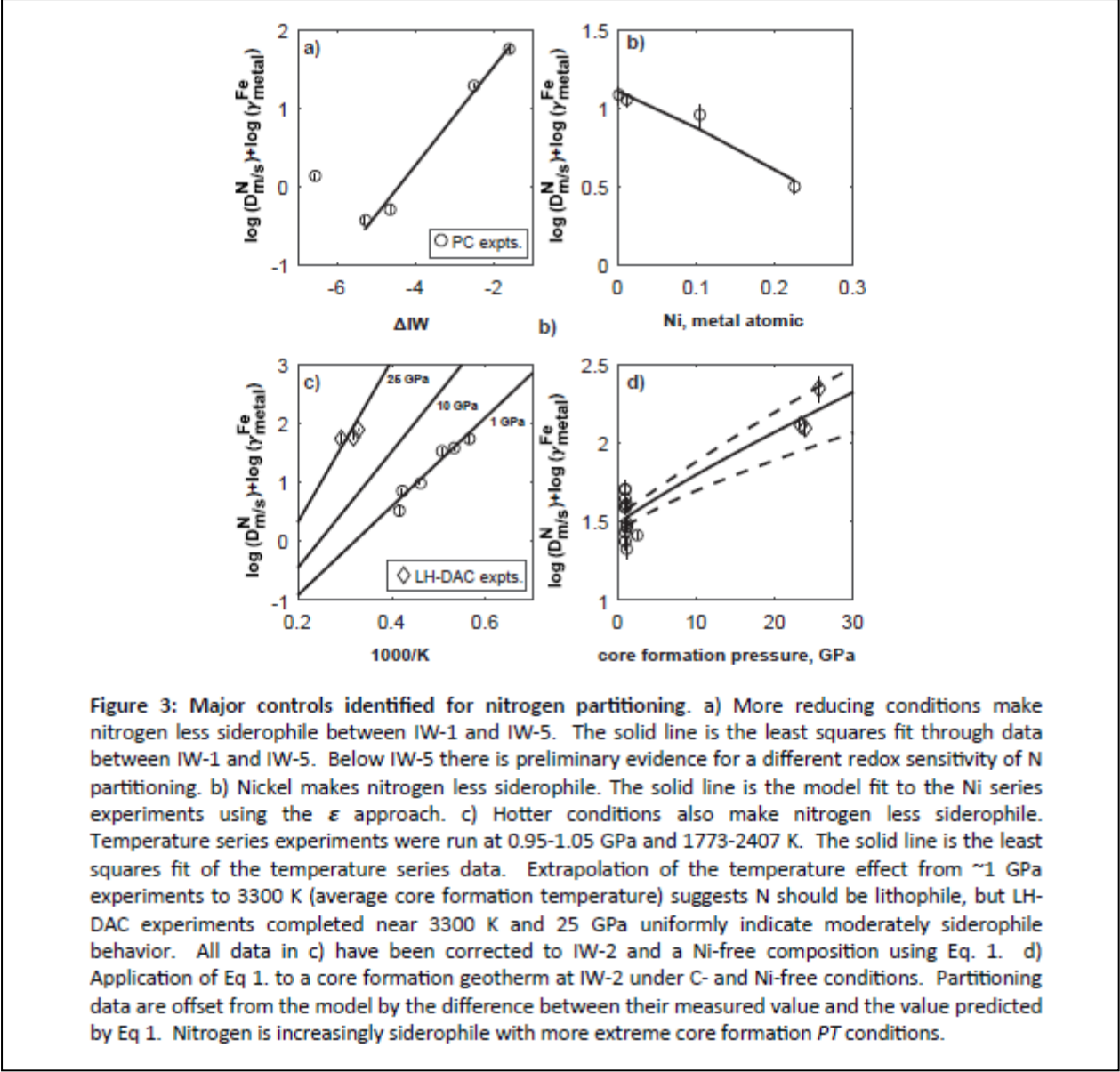
89 Figure 2 provides an example BSE (backscattered electron) image and *T-time* path for a LH-DAC
90 heating spot. The bright, circular phase is the quenched Fe alloy which is in contact with the
91 darker, quenched silicate liquid. The heating spot is surrounded by ferropericlase. The dark
92 inclusions are C-rich, indicating C-saturation for this particular experiment. Experimental
93 conditions are reported in Table 1 and Supplementary Table 1. Starting compositions for silicate
94 materials are reported in Supplementary Table 2.

95 We quantified the composition of reacted metal and silicate pairs using field-emission electron
 96 microprobes at the Smithsonian and Carnegie Institutions. Nitrogen analyses were completed using a
 97 LDE1L crystal, 10 kV accelerating voltage, and either 75-80 nA or ≤ 5 nA beam currents for piston cylinder
 98 or LH-DAC experiments, respectively. Silicon nitride was used as the standard (MTI Corporation) for N
 99 analysis, following the approach of 23. No evidence for N mobility under the electron beam was
 100 observed, in agreement with other studies of N partitioning that employed similar analytical techniques
 101 ^{23,25}.



102 We completed independent series of experiments to quantify the P - T - X controls on N
 103 partitioning between liquid metal and silicate ($D_{m/s}^N = [X_N^{metal}]/[X_N^{silicate}]$, atomic fraction, Figure 3,
 104 Supplementary Table 1, Supplementary Figures 1 and 2). Individual series correlations indicate $D_{m/s}^N$
 105 values depend strongly on oxygen fugacity (fO_2) ($R^2 = 0.99$, p-value = 0.005, n = 4) and temperature ($R^2 =$
 106 0.97 , p-value = 0.001, n = 6) over conditions relevant to magma oceans (Figure 3a and 3c), whereas
 107 X_{metal}^C , X_{metal}^{Ni} , and ionic porosity of silicate liquid have significant (p-values <0.05) but relatively minor
 108 effects (Figure 3b, Supplementary Figures 1 and 2). Our fO_2 and temperature findings accord with

109 previous work²⁴⁻²⁶. We also find that X_{metal}^S has a negative effect on $D_{m/s}^N$ values, but this effect is not
 110 significant at the 95 % confidence level in our dataset (p-value = 0.12, Supplementary Figure 2). The
 111 negative influence of S on $D_{m/s}^N$ values suggested by our data is qualitatively consistent with the finding
 112 of 25.



113 Our primary result is that $D_N^{m/s}$ values strongly increase as a function of pressure (P/T), as
 114 indicated by the offset between PC (1 GPa) and LH-DAC data (~ 25 GPa) in Figure 3c. This result implies
 115 that core formation under the $P-T$ conditions associated with larger terrestrial planets, such as Earth, is

116 an efficient mechanism to increase S/N and C/N ratios in observable reservoirs by preferentially
117 sequestering N to the core. Previous work has also identified that $D_{m/s}^N$ values increase with pressure
118 (P/T)^{20,24,25}, but experiments were limited to more moderate conditions and application to core
119 formation in Earth required correspondingly large pressure extrapolation.

120 To parameterize our data, we first recalculate all experiments to a carbon-free baseline using
121 the interaction parameter ($\varepsilon_C^N = 5.9 \pm 1.9$) determined by the negative correlation between carbon
122 content of Fe alloy at carbon saturation and $X_{metal}^{\varepsilon N}$ ($R^2 = 0.70$, p-value 0.01, n = 7, Supplementary Figure
123 1). The positive interaction parameter indicates that C lower $D_{m/s}^N$ values, consistent with previous work
124^{24,27}. We then conduct an equal-weight, multiple least squares regression on parameters identified as
125 significant in their individual series ($1/T$, P/T , X_{metal}^{Ni} , and ΔIW). This regression does not include ionic
126 porosity series experiments as the effect of ionic porosity in silicate melt in promoting neutral species
127 solubility at pressure remains uncertain. Our approach yields the following expression ($R^2 = 0.95$, p-
128 value <0.001, n = 16):

$$129 \ln(D_{m/s}^{N, C-free}) = 16823 \pm 2297 \ 1/T + 594 \pm 77 \ P/T + 5.0 \pm 1.3 \ X_{metal}^{\varepsilon Ni} + 1.33 \pm 0.08 \ \Delta IW - \\ 130 2.93 \pm 1.16 - \ln(\gamma_{metal}^{Fe}) \text{ (Eq .1)}$$

131 All coefficients have p-values equal lower than 0.05. All uncertainties are reported as 1σ .
132 Temperature and P/T effects overlap at the 2σ limit on individual terms reported by 25. Note that
133 $X_{metal}^{\varepsilon Ni}$ refers to the expanded concentration expression associated with the ε notation of 34 and that
134 positive coefficients indicate negative effects on partitioning. Application of Eq. 1 to a mantle liquidus
135 geotherm³⁵ at IW-2 indicates a monotonic increase in $D_{m/s}^N$ with depth (Figure 3d). Additional details
136 regarding this regression, including the calculation of the C effect, fO_2 , and γ_{metal}^{Fe} , as well as individual
137 experiment series correlations, are provided in the Supplementary Information. The covariance matrix
138 for parameters in Eq. 1 is reported in Supplementary Table 3.

139 We apply Eq. 1 to literature data to validate its predictive power (Supplementary Figure 3). We
140 predict literature data ^{20,22,25,26} (n = 105, excludes S-bearing experiments and experiments with Si-
141 bearing alloy from 25) with an R² value of 0.82. The strong correlation implies Eq. 1 is a robust
142 description of N partitioning over a wide range of conditions. Residuals between $D_{m/s}^N$ values predicted
143 from Eq. 1 and literature $D_{m/s}^N$ values from multiple studies do not correlate with pressure (R² = 0.01, p-
144 value = 0.29), supporting the relatively strong pressure effect identified by our experiments. The
145 pressure and temperature conditions reported for LH-DAC experiments are verified using their metal-
146 silicate partitioning of Ni, Mg, and Si (Supplementary Figure 4).

147 **Parameterization of metal-silicate partitioning data for sulfur**

148 Having established the predictive power of Eq. 1 and that pressure exerts strong changes in
149 $D_{m/s}^N$ values over conditions relevant to core formation in terrestrial planets, we now parameterize $D_{m/s}^S$
150 in order to predict for how core formation at higher *P-T* conditions modulates (S/N)_{OE} ratios. Our
151 parameterization includes high *P-T* data ^{18,30-32} (12-91 GPa, 2600-4900 K, n = 36). We take a stepwise
152 approach to parameterize $D_{m/s}^S$ values (Supplementary Figure 5). We first include *1/T* and *P/T* terms.
153 The next most significant term is $X_{metal}^{\epsilon C}$ (P-value <0.001). No other terms were significant at the 95%
154 confidence level. Including a $X_{silicate}^{FeO}$ term yields a value of -3.8, a value consistent with Fe-S
155 complexation in silicate melt. The p-value for the $X_{silicate}^{FeO}$ term, however, is 0.09, and we consequently
156 do not include it. Our approach yields the following expression (R² = 0.78, n = 36):

$$157 \ln(D_{m/s}^S) = 8377 \pm 2762 \, 1/T - 123 \pm 24 \, P/T + 10.3 \pm 2.0 \, X_{metal}^{\epsilon C} + 3.69 \pm 1.03 - \ln(\gamma_{metal}^{Fe})$$

158 (Eq .2)

159 The combined dataset provides a continuous constraint on $D_{m/s}^S$ values up to 90 GPa and
160 indicates that S is only moderately siderophile at the mean pressure of Earth's core formation, 30-59

161 GPa^{28,29}. The covariance matrix for parameters in Eq. 2 is reported in Supplementary Table 3.
162 Importantly, this expanded high pressure dataset is consistent with the gradual decrease in $D_{m/s}^S$ values
163 with increasing P - T conditions along a magma ocean geotherm, as originally suggested by 30.

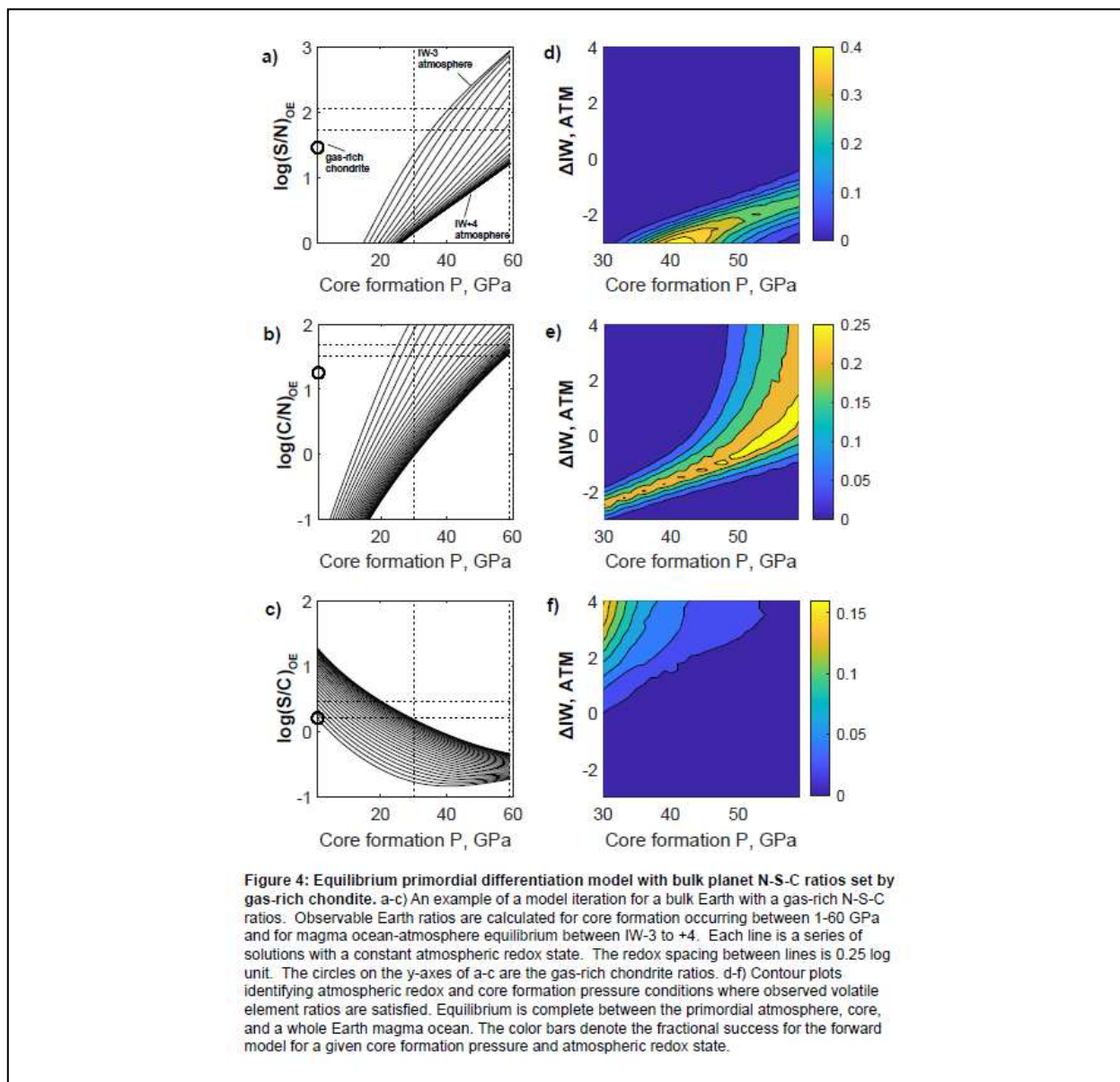
164 We use the $D_{m/s}^C$ parameterization from 33 (EMPA data) to predict the response of C to core
165 formation. Core oxygen content affects $D_{m/s}^C$ values, and estimates for core oxygen content range
166 between ~2 and 5 wt % (~7-17 mol %) ^{29,36}. We take 9 mol % as a nominal concentration and explore
167 model sensitivity to changes about this value in the Supplement (Supplementary Figure 6). Carbon is
168 highly volatile such that much of a planet's C budget may initially reside in its atmosphere. To account
169 for this, we calculate the solubility of C in a bulk silicate Earth composition magma in under oxidizing
170 conditions (0.04 mol C/g-bar, >IW+3) using the CO₂ solubility model of 37, and we combine this
171 calculation with C solubility estimates for more reduced conditions from 6. We then parameterize C
172 solubility in magma as a function of fO_2 using a second-order polynomial.

173 The combined dynamic is that C and S both become less siderophile, while N become more
174 siderophile, with increasing P - T conditions. At the same time, C becomes less volatile, while N becomes
175 more volatile as atmospheric conditions become more oxidizing. Sulfur is not volatile under these
176 geologic conditions ³⁸, and its bulk Earth distribution is not therefore sensitive to the nature of the
177 primordial atmosphere.

178 **Modeling observable N-S-C ratios of planets in response to primordial differentiation**

179 We seek to identify forward models of primordial differentiation that satisfy the following
180 constraints: 1) the $(S/N)_{OE}$ ratio is 82 ± 28 ⁶, 2) the $(C/N)_{OE}$ ratio is 40 ± 8 ⁶, 3) the $(C/S)_{OE}$ ratio is $0.49 \pm$
181 0.14 ⁶, and 4) the single-stage pressure of core formation falls between 30 and 59 GPa, the range of
182 conditions independently identified to satisfy the moderately siderophile element abundances of the
183 mantle ^{28,29}. Temperatures are fixed at the liquidus of mantle ³⁵, and core-mantle equilibrium fO_2 is fixed

184 to IW-2, the redox potential that reproduces the current FeO content of the silicate Earth. We
 185 additionally allow atmospheric fO_2 conditions to vary between IW-3 to IW+4. We take a single-stage
 186 approach because it has relatively few free parameters so that the connection between the P - T - X
 187 conditions that a planet experiences during differentiation and planetary chemistry is highlighted.



188 Our forward modeling of primordial differentiation, which includes core formation and
 189 primordial atmosphere degassing, takes the following form (Figure 4a-c): Pressures are varied from 1-60
 190 GPa and $D_{m/s}^S$ values calculated following Eq. 2. We explore the larger range of pressure to fully

191 document the expected N-S-C systematics for planets in general. We assume the magma ocean contains
192 225 ± 25 ppm, as constrained by modern concentrations in bulk silicate Earth ⁶, and $D_{m/s}^S$ values are
193 applied to determine a bulk sulfur content of the Earth over the range of considered pressures. Core and
194 mantle mass remain fixed at 32.5 and 67.5 %, respectively. Bulk Earth sulfur contents (mantle+core)
195 range between ~ 8000 (30 GPa solutions) and ~ 2000 (59 GPa solutions) ppm. Both values are near bulk
196 Earth S content inferred from the volatile depletion trend of 5600 ppm ³⁹. We then calculate bulk Earth
197 nitrogen and carbon contents as a function of sulfur content using the S/N and C/N ratios from different
198 groups of chondrites ⁷.

199 For each core formation pressure evaluated, we also explore the effect of atmospheric fO_2
200 (IW+4 to IW-3) as an independent variable (Figure 4a-c). Variations in atmospheric state may be driven
201 by changes in ferric iron stability with pressure ^{40,41} and can lead to more reducing or more oxidizing
202 shallow conditions compared to that associated with metal-magma reactions at depth. Atmosphere fO_2
203 is important for N and C because their volatility also depends on their dominant valence state. Thus,
204 much of a planet's initial carbon and nitrogen budget can reside the atmosphere, but the exact fraction
205 depends on the fO_2 under which magma oceans and atmospheres equilibrate.

206 Mass balance of N, S, and C between the atmosphere, magma ocean, and core is then calculated
207 for the imposed P - T -atmospheric fO_2 conditions. Atmospheric and magma ocean reservoirs combine to
208 create the observable Earth. Results are evaluated to determine if the resulting $(S/N)_{OE}$, $(C/N)_{OE}$, and
209 $(C/S)_{OE}$ ratios are within the allowable ranges ⁶ and core formation pressure is between 30-59 GPa, or
210 the range permitted by refractory siderophile elements ^{29,30}. If it is, then this model is identified as
211 successful and conditions are logged (Figure 4d-f).

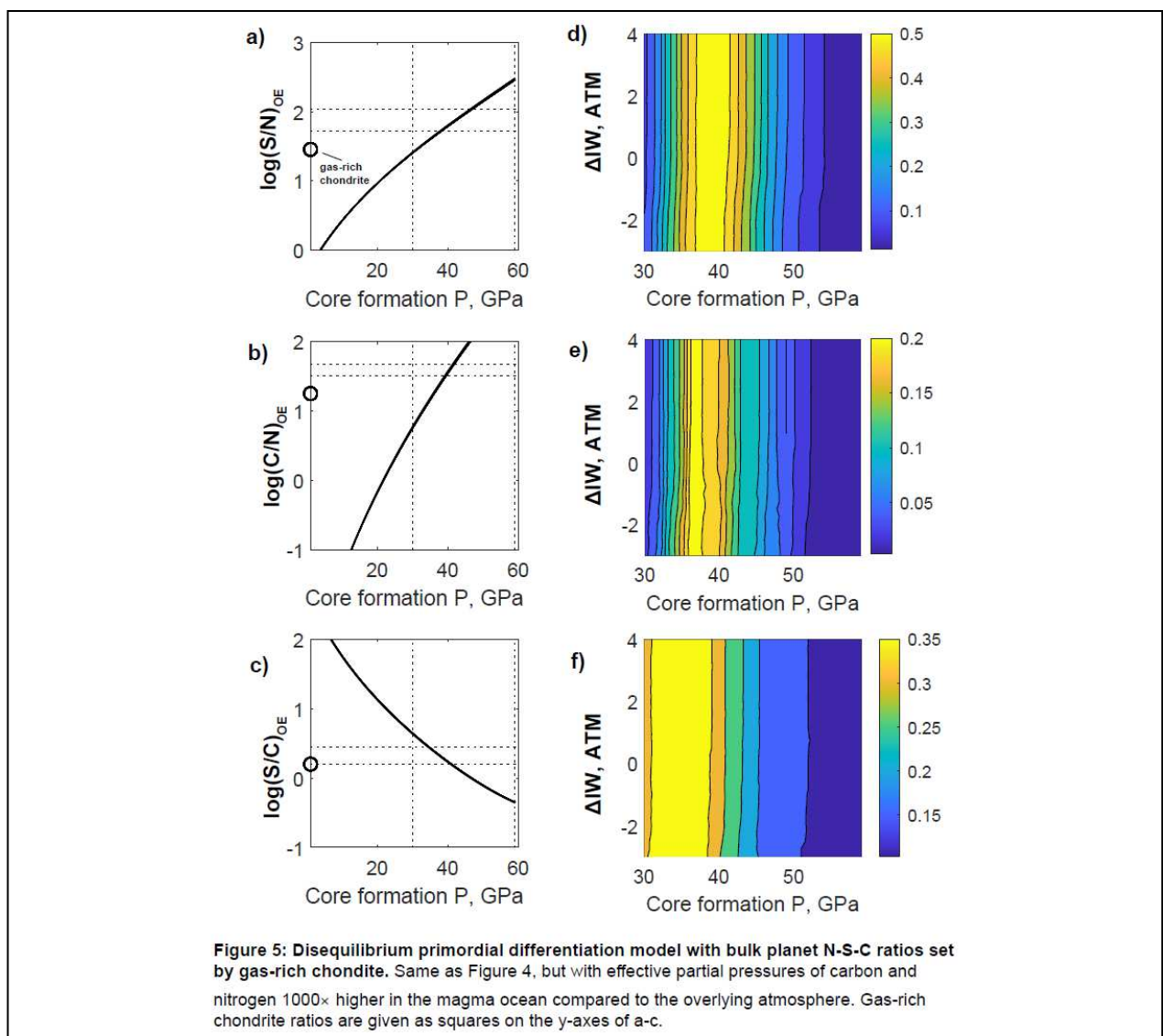
212 Figures 4a-b plot the results for a single iteration through all explored core formation pressures
213 and atmospheric fO_2 conditions for a model with bulk N-S-C ratios of gas-rich chondrite. Calculated

214 $(S/N)_{OE}$, $(C/N)_{OE}$, and $(C/S)_{OE}$ ratios are plotted as function of core formation pressure. Dotted horizontal
215 and vertical lines delineate the range of potentially successful solutions. Nitrogen largely remains in the
216 atmosphere-magma ocean system, while C and S largely remain in the core under lower pressure
217 conditions. This behavior leads to starkly depressed $(S/N)_{OE}$ and $(C/N)_{OE}$ ratios early in the process of
218 core formation. With pressure, the situation reverses. Nitrogen is drawn into the core while S and C are
219 drawn into the mantle, with some C also outgassing to the atmosphere. This causes $(S/N)_{OE}$ and $(C/N)_{OE}$
220 ratios to rise. Uncertainties in $D_{m/s}^N$, $D_{m/s}^S$, and $D_{m/s}^C$ values are propagated into the model by varying
221 the respective fitting parameters according to their covariance matrices between 1000 iterations
222 (Supplementary Table 3 and ref. 33).

223 Figures 4d-f plot successful primordial differentiation conditions for Earth where its bulk N-S-C
224 ratios are set by gas-rich chondrite. Warmer colors indicate conditions with a higher rate of model
225 success. Bulk Earth contains 65-350 PAN (PAN = present atmospheric nitrogen abundance) between
226 various successful models. To draw this large amount of N away from the atmosphere-magma ocean
227 system while also satisfying the $(S/N)_{OE}$ ratio, a reduced atmosphere (<IW) overlying a deep magma
228 ocean (high pressure core formation) appears required, opposite to recent predictions stemming from
229 the pressure-dependence of Fe^{+3} - Fe^{+2} equilibria^{40,41}. Satisfying $(C/S)_{OE}$ ratios, on the other hand,
230 requires oxidizing atmospheric conditions. The net result is that there is not common primordial
231 differentiation scenario that co-satisfies the combined N-S-C constraint given that Earth's volatile
232 elements were delivered by gas-rich chondrites. This statement essentially holds true even if we vary
233 the O content of the core (Supplementary Figure 6) or introduce small amounts of disequilibrium
234 between the magma ocean and overlying atmosphere (Supplementary Figure 7).

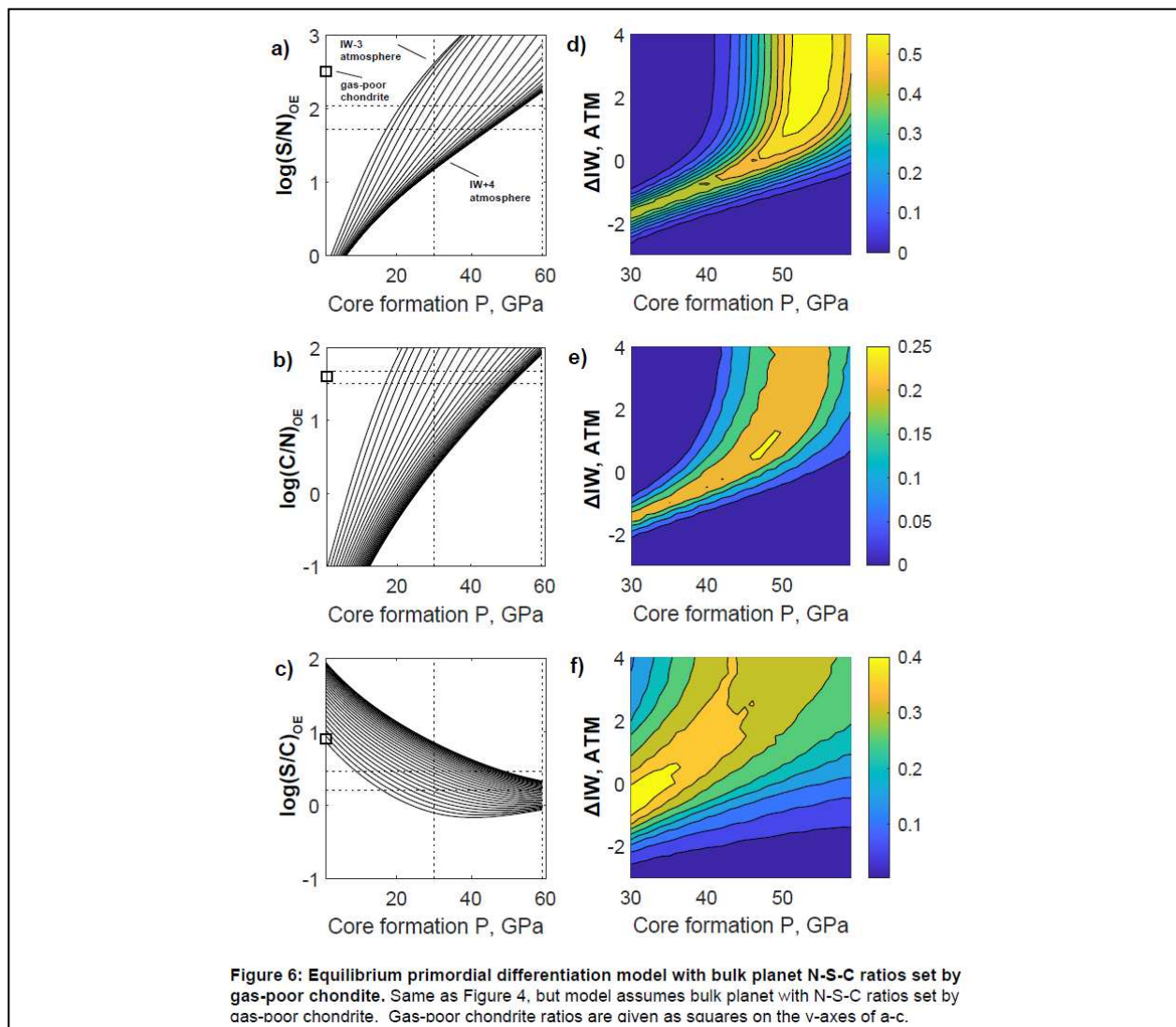
235 We do, however, find overlapping N-S-C solutions if we consider core formation to be fast
236 compared to magma ocean outgassing time-scales⁴². In this case core formation could occur in a
237 magma ocean with a high concentration of undegassed volatile elements. We model this by increasing

238 the effective partial pressure of C and N in the magma ocean to be much larger than their actual
 239 pressures in the overlying atmosphere (effective partial pressure is the pressure of gas required to
 240 dissolve the concentration of the corresponding element in the magma ocean). Figure 5 plots our model
 241 results assuming effective partial pressures for C and N are 1000× their equilibrium values, essentially
 242 forcing the magma ocean to the sole reservoir of the observable Earth. A common solution for $(S/N)_{OE}$,
 243 $(C/N)_{OE}$, and $(C/S)_{OE}$ ratios is found at moderate pressure (~35-40 GPa) that is independent of
 244 atmospheric fO_2 , as little gas is present in the atmosphere for these scenarios.



245 It is not required, however, that bulk Earth volatile element ratios are directly set by gas-rich
 246 chondrites. Other types of chondrites, or relatively devolatilized materials, may have been more
 247 influential in delivering volatiles to Earth ¹⁰⁻¹². This raises the question of whether primordial
 248 differentiation processes can successfully combine to account for $(S/N)_{OE}$, $(C/N)_{OE}$, and $(C/S)_{OE}$ ratios if a
 249 degree of N and C depletion is inherent to Earth as a bulk system ^{e.g. 11}.

250 To address this question, we extend our modeling approach to include bulk Earth N-S-C ratios
 251 set by gas-poor chondrites ⁷ (average of CO, CV, H, L, and LL groups) – materials with depletions of
 252 nitrogen and carbon relative to sulfur (Figure 1). Here, successful primordial differentiation models must
 253 decrease $(S/N)_{OE}$ ratios from a bulk value of 323 to 82 ± 28 , while $(C/N)_{OE}$ ratios must remain essentially
 254 unchanged (Figure 1).



255 We indeed find that primordial differentiation processes can co-satisfy $(S/N)_{OE}$, $(C/N)_{OE}$, and
256 $(C/S)_{OE}$ ratios with bulk system N-S-C ratios set by gas-poor chondrites (Figure 6). Success here is found
257 where magma oceans and primordial atmospheres equilibrate, making the atmosphere a significant
258 component for observable budget of N and C. This contrasts the successful solutions identified for gas-
259 rich chondrites (Figure 5), where MOs had relatively high effective partial pressures and little gas was
260 correspondingly present in the atmosphere at the point of core formation. Success in gas-poor
261 chondrite models is most commonly achieved with a relatively oxidizing atmosphere, but a set of
262 common solutions extends to more reduced atmospheres and lower pressure core formation (Figure 6d-
263 f). Complete core-magma ocean-atmosphere equilibrium is assumed, but better overlap of $(S/N)_{OE}$,
264 $(C/N)_{OE}$, and $(C/S)_{OE}$ solutions can be achieved by allowing for relatively minor core-magma ocean-
265 atmosphere disequilibrium and by varying the oxygen content of the core (Supplementary Figures 6 and
266 7). Nonetheless, the essential result remains the same after optimizing overlap within gas-poor
267 chondrite scenarios – oxidizing atmospheres that equilibrate with their underlying magma ocean
268 provide the broadest and most likely set of solutions.

269 The success of core formation and an oxidized atmosphere setting $(S/N)_{OE}$, $(C/N)_{OE}$, and $(C/S)_{OE}$
270 ratios given a gas-poor bulk Earth (Figure 6) is consistent with the recent predictions of magma ocean
271 fO_2 profiles with depth^{40,41}, where deep magma oceans are expected to co-exist with oxidized
272 atmospheres.

273 Discussion

274 A unifying point is that primordial differentiation processes are highly efficient in redistributing
275 volatile elements throughout planets (Figures 4-6). We can account for Earth's N-S-C systematics by
276 simply combining the natural variability of chondrites, materials that are commonly associated with
277 volatile element delivery to terrestrial planets, primordial differentiation processes that are known to
278 occur, and the independently constrained P - T - X conditions for average core formation that satisfy

279 refractory element constraints^{28,29}. Our findings hold if we were to subtract the late veneer from the
280 observable Earth volatile budget. This is because the late veneer supplies only ~10 % of observed N, S,
281 and C, assuming it was dominated by gas-poor chondrites, as suggested by Mo-Ru systematics⁴³.

282 Solution fields show the strong combined influence of atmospheric fO_2 and core formation P - T
283 conditions in modulating observable volatile budgets (Figures 4-6). This is important because it suggests
284 that the specific, and likely highly variable⁴⁴, conditions that a planet experiences during its growth and
285 primordial differentiation strongly affects its later surface conditions, habitability, and geologic
286 evolution. Planets are not passive recipients of their life-enabling and climate-modifying elements.

287 Our model also makes general predictions for observable C/N ratios for planets of varying size, a
288 parameter that can be remotely constrained through atmospheric observations. Larger planets have
289 higher average pressures of core formation, all other things being equal, and will have higher observable
290 C/N ratios due to the opposing effects of pressure on $D_{m/s}^N$ and $D_{m/s}^C$ values (Figures 4-6b). Mars is the
291 smallest planet in the Solar System and the only planet beyond Earth with firm estimates for core
292 formation pressure along with volatile budget constraints. As introduced above, Mars's atmosphere
293 provides evidence that its observable C/N ratio is near or below the gas-rich chondrite (Figure 1b). Our
294 model predicts this, given the low core formation pressure that Mars experienced, ~14 GPa⁴⁵, although
295 the atmospheric C/N ratio of Mars is biased toward relatively modern inputs, as N is rapidly lost to space
296¹⁵ and most C is sequestered in early-forming carbonate and ice⁴⁶. Venus, which is intermediate in mass
297 to Earth and Mars, and presumably experienced core formation at a pressure intermediate to Earth and
298 Mars, has an atmospheric C/N ratio that is also intermediate to Earth and Mars. The comparison
299 between Earth and Venus is more direct in that the Venusian atmosphere appears to be closed with
300 respect to N- or C-loss and carbonates are likely unstable⁴⁷. The support that Mars and Venus lend to
301 our model strengthens the hypothesis that primordial differentiation is a dominant process in
302 modulating observable volatile budgets of planets in general. The link between planet mass and the

303 distribution of volatiles throughout planets should enable more precise evaluations of exoplanet
304 habitability, worlds for which size remains a central constraint on their geologic evolution.

305

306 **Methods**

307 **Experimental Design**

308 We conducted lower P - T partitioning experiments using a piston cylinder (PC) and higher P - T
309 experiments using a laser-heated diamond anvil (LH-DAC) cell. PC experiments ($P = 0.95$ - 2.38 GPa, $T =$
310 1773 - 2413 K) primarily target the effect of temperature, fO_2 , X_{metal}^C , X_{metal}^S , and, X_{metal}^{Ni} . LH-DAC
311 experiments ($P = 23.8$ - 25.6 GPa, $T = 3046$ - 3436 K) target the effect of pressure (P/T).

312 **Piston cylinder method**

313 We used graphite capsules in all PC experiments loaded with equal weights of silicate oxide
314 power and Fe alloy components. Alloying components include Fe metal, FeSi alloy, FeNi alloy, and Fe-
315 nitride ($Fe_{2-4}N$). Alloy components were varied to control X_{metal}^{Ni} and experimental fO_2 . The silicate
316 oxide powder composition is basaltic with the exception of experiments designed to test the effect of
317 ionic porosity. Starting silicate compositions were glassed and their compositions are reported in
318 Supplementary Table 2. Titanium oxide was not included to eliminate the interference of Ti on N during
319 electron microprobe, and Na was replaced for K.

320 We used $BaCO_3$ pressure media, straight-walled graphite furnaces, crushable MgO spacers, and
321 D-type thermocouples in all PC experiments. Spacers were machined to position capsules in the hotspot
322 of the assembly, and a 1 mm MgO disk was placed above the capsule to prevent thermocouple
323 contamination. Graphite capsules were contained within an Al_2O_3 annulus to provide insulation from
324 the furnace, maintain geometry upon compression, and to smooth temperature gradients along the axis
325 of the capsule. Experiments were compressed to near the run pressure, ramped by 100 K/min to 1073
326 K, and annealed for >1 hour to help maintain the integrity of the graphite capsules after melting.

327 Experiments were then ramped by 150 K/min to the run temperature while maintaining pressure (hot
328 piston in). All experiments were completed at superliquidus conditions. Power consumption was
329 monitored at the experimental temperatures as a check for thermocouple contamination. Experiments
330 were quenched if power consumption started to systematically vary. Experiments were quenched by
331 cutting the electrical current to the furnace and pressure was held during the quench. Run durations
332 ranged from 1 minute to 3.25 hours, with shorter experiments generally being correspondingly hotter.
333 We assume a 5% friction correction for PC experiments with BaCO₃ pressure media. Temperature
334 uncertainty is assumed to be 10 K and pressure uncertainty is assumed to be 0.05 GPa.

335 **LH-DAC method**

336 LH-DAC experiments constrain the pressure effect on nitrogen partitioning during core
337 formation. Experimental methods follow those outlined in 31 with several exceptions. Starting materials
338 were ball-milled to generate a fine-grained, intimate mixture of metal and silicate. This mixture was
339 pressed into a sample chamber cut into a preindented Re gasket (~20 μm) using stepped anvils. We
340 then placed foils of MgO powders above and below the pressed metal+silicate mixture. These foils
341 provide thermal insulation for the heating spots from the diamond anvils and buffer the melt to
342 geologically applicable compositions. Diamond cells with loaded gaskets were then placed in a vacuum
343 oven and heated overnight to remove adsorbed water. Nitrogen was introduced into the DAC by a gas
344 loading system. To ensure a pure N₂ atmosphere was introduced, a vacuum was first drawn and then
345 the gas-loading system was purged with N₂. Starting materials were a metal-oxide mixture with a bulk
346 composition of C1/C from 48.

347 We conducted laser heating at 13-ID-D GSECARS, Advanced Photon Source. Emission spectra
348 were monitored on both sides to constrain the temperature of metal-silicate reaction. Experiment
349 temperatures were determined by fitting emission spectra and taking the average of the hotter side in

350 the final series of measurements prior to quench. Quoted temperature uncertainties are the standard
351 deviation of the final temperature measurement series average. Pressure is calculated using the
352 equation of state for MgO⁴⁹ applied at the measured experimental temperature and volume of MgO
353 observed in the experiments, as constrained by x-ray diffraction. Quoted pressure uncertainties include
354 the fractional uncertainty on the temperature, multiplied by the nominal pressure plus an analytical
355 uncertainty of 2 GPa.

356 **Sample preparation**

357 PC experiment charges were sectioned in half using a diamond wafering blade. The cut surface
358 was rough polished using SiC sandpaper using water as the lubricant. Fine polish was achieved using
359 diamond paste using turbinoid as the lubricant. Turbinoid was used during final polishing to limit
360 surface oxidation of the Fe alloy prior to chemical analysis.

361 A laser cutter was used to liberate the sample chamber of LH-DAC experiments from the
362 remaining gasket. The sample chamber was then loaded onto a TEM grid that was held in place by a
363 custom machined sample post. Heating spots within the sample chamber were exposed for chemical
364 analysis using a focused ion beam (Ga⁺). Final polishing was completed using a 30 kV, 1 nA beam. All
365 samples were Ir coated to facilitate carbon analysis in the Fe alloy phase.

366 **Electron Microprobe Analysis**

367 Elemental concentrations of glass and Fe alloy phases were determined by electron microprobe
368 analysis. Standards were as follows: manganite (Mn), diopside (Ca), chromite (Cr), enstatite (Si and Mg),
369 anorthoclase (Al and Na), microcline (K), Fe₅₀Ni₅₀ alloy (Ni), pyrite (S), tungsten carbide (C), silicon nitride
370 (N), iron metal (Fe in metal), augite (Fe in silicate analyses), Re metal (Re). A ZAF matrix correction was
371 used. Analytical conditions were 10 kV, 75-80 nA, and 10 μm diameter electron beam for piston cylinder
372 experiments. Analytical conditions were 10 kV, <5 nA, and 1-3 μm diameter electron beam for LH-DAC

373 experiments. A 10 kV beam was used to minimize matrix corrections on nitrogen. Nitrogen was
 374 analyzed using an LDE1L crystal. An exponential model was used for nitrogen to account the background
 375 curvature local to the nitrogen peak on the LDE1L crystal. Counting times were 90 s on peak and 60 s off
 376 peak for nitrogen. The remaining elements were analyzed for 30 s on peak and 15 s off peak. Repeat
 377 analysis of the basaltic starting composition glass for PC series experiments yields an N concentration of
 378 0.004 ± 0.005 wt % (Supplementary Table 2). Background models for all other elements were linear.

379 **Oxygen fugacity calculation**

380 We calculate fO_2 with respect to the IW buffer using measurements of [Fe] and [FeO] in metal
 381 and silicate, respectively, using the following equation:

$$\Delta IW = 2 \log (X_{silicate}^{FeO} \cdot \gamma_{silicate}^{FeO} / X_{metal}^{Fe} \cdot \gamma_{metal}^{FeO})$$

382 (Eq. 3)

383 Activity coefficients for FeO ($\gamma_{silicate}^{FeO}$) are calculated according to the parameterization of 50. We scale
 384 $\gamma_{silicate}^{FeO}$ calculations for temperature:

$$\ln (\gamma_{silicate}^{FeO})@ T_{experiment} = \ln (\gamma_{silicate}^{FeO}) \cdot \frac{1673}{T_{experiment}}$$

385 (Eq. 4)

386 Activity coefficients for Fe (γ_{metal}^{Fe}) are calculated following the formalism outlined in 34 for the
 387 interactions between O, S, and C. Interaction parameters are taken from 51 with several exceptions.
 388 Exceptions are as follows: ϵ_O^C and ϵ_O^O values are from 29 and the ϵ_O^S value is calculated from the
 389 partitioning data of 52 ($\epsilon_O^S = -2.2$).

390 **Parameterization of non-ideal solution behavior for nitrogen in liquid Fe-alloy**

391 Our approach to parameterizing non-ideal solution behavior for Fe-alloy follows from recent
 392 studies e.g. 28,29,31,53. Alloying components in Fe metal alter the solution properties of N with
 393 corresponding effects on partitioning e.g.,²⁵. Variations in the solution properties for N are quantified
 394 using the activity coefficient of N dissolved into Fe metal or γ_{metal}^N . Here γ_{metal}^N is parameterized
 395 following the formalism outlined in 34 modified to not include the activity coefficient at infinite dilution
 396 (γ_{N^0}) or nitrogen self interaction parameter (ϵ_N^N):

$$\ln(\gamma_{metal}^N) = \sum \epsilon_N^i X_{metal}^{i\epsilon}$$

397 (Eq. 5)

398 where $X_{metal}^{i\epsilon} = T_{ref}/T_{expt}$. $[X_{metal}^i \left(1 + \frac{\ln(1-X_{metal}^i)}{X_{metal}^i} - \frac{1}{1-X_{metal}^N}\right) - X_i^{metal^2} X_N^{metal} \left(\frac{1}{1-X_{metal}^N} + \right.$
 399 $\left. \frac{1}{1-X_{metal}^i} + \frac{X_{metal}^N}{2(1-X_{metal}^N)^2} - 1\right)]$ for $i = C, S, \text{ or } Ni$ (Eq. 6)

400 Fitting the $1/T$ term in Eq. 1 indirectly accounts for γ_{N^0} , and a stepwise fit of partitioning data does not
 401 identify ϵ_N^N as significantly correlated with N partitioning, suggesting its effect is small within the
 402 presently explored range of X_{metal}^N values. We assume that $X_{metal}^{i\epsilon}$ scales with inverse temperature and
 403 the reference temperature is 1873 K.

404

405 References

- 406 1) Alexander, C. O. D., Bowden, R., Fogel, M., Howard, K., Herd, C. and Nittler, L., The
 407 provenances of asteroids, and their contributions to the volatile inventories of the
 408 terrestrial planets, *Science*, 337(6095), pp. 721-723 (2012).
 409 2) Marty, B., The origins and concentrations of water, carbon, nitrogen and noble gases
 410 on Earth, *Earth and Planetary Science Letters*, 313, pp. 56-66 (2012).
 411 3) Labidi, J., Cartigny, P. and Moreira, M. Non-chondritic sulphur isotope composition of
 412 the terrestrial mantle, *Nature*, 501(7466), pp. 208 (2013).
 413 4) Hirschmann, M. M. and Dasgupta, R. The H/C ratios of Earth's near-surface and deep
 414 reservoirs, and consequences for deep Earth volatile cycles, *Chemical Geology*,
 415 262(1-2) (2009).
 416 5) Halliday, A. N. The origins of volatiles in the terrestrial planets', *Geochimica Et*
 417 *Cosmochimica Acta*, 105, pp. 146-171 (2013).

- 418 6) Hirschmann, M. M. Constraints on the early delivery and fractionation of Earth's major
419 volatiles from C/H, C/N, and C/S ratios, *American Mineralogist*, 101(3), pp. 540-553
420 (2016).
- 421 7) Wasson, J. T. and Kallemeyn, G. W. Compositions of chondrites, *Philosophical*
422 *Transactions of the Royal Society of London. Series A, Mathematical and Physical*
423 *Sciences*, 325(1587), pp. 535-544 (1988).
- 424 8) Libourel, G., Marty, B. and Humbert, F. 'Nitrogen solubility in basaltic melt. Part I.
425 Effect of oxygen fugacity, *Geochimica Et Cosmochimica Acta*, 67(21), pp. 4123-4135
426 (2003).
- 427 9) Tucker, J. M. and Mukhopadhyay, S. Evidence for multiple magma ocean outgassing
428 and atmospheric loss episodes from mantle noble gases, *Earth and Planetary Science*
429 *Letters*, 393, pp. 254-265 (2014).
- 430 10) Schlichting, H. E., Sari, R. e. and Yalinewich, A. Atmospheric mass loss during planet
431 formation: The importance of planetesimal impacts, *Icarus*, 247, pp. 81-94 (2015).
- 432 11) Bergin, E. A., Blake, G. A., Ciesla, F., Hirschmann, M. M. and Li, J. Tracing the
433 ingredients for a habitable earth from interstellar space through planet formation,
434 *Proceedings of the National Academy of Sciences*, 112(29), pp. 8965-8970 (2015).
- 435 12) Raymond, S. N., Quinn, T. and Lunine, J. I. Making other earths: dynamical
436 simulations of terrestrial planet formation and water delivery, *Icarus*, 168(1), pp. 1-17
437 (2004).
- 438 13) Owen, T. and Biemann, K. Composition of the atmosphere at the surface of Mars –
439 detection of ³⁶Ar and preliminary analysis, *Science*, 193(4255), pp. 801-803 (1976).
- 440 14) Lécuyer, C., Simon, L. and Guyot, F. Comparison of carbon, nitrogen and water
441 budgets on Venus and the Earth', *Earth and Planetary Science Letters*, 181(1-2), pp.
442 33-40 (2000).
- 443 15) McElroy, M. B., Kong, T. Y. and Yung, Y. L. Photochemistry and evolution of Mars'
444 atmosphere: A Viking perspective, *Journal of Geophysical Research*, 82(28), pp. 4379-
445 4388 (1977).
- 446 16) Clesi, V., Bouhifd, M. A., Bolfan-Casanova, N., Manthilake, G., Schiavi, F., Raepsaet,
447 C., Bureau, H., Khodja, H. and Andrault, D. (2018) 'Low hydrogen contents in the
448 cores of terrestrial planets', *Science advances*, 4(3), pp. e1701876.
- 449 17) Iizuka-Oku, R., Yagi, T., Gotou, H., Okuchi, T., Hattori, T. and Sano-Furukawa, A.
450 (2017) 'Hydrogenation of iron in the early stage of Earth's evolution', *Nature*
451 *communications*, 8(1), pp. 1-7.
- 452 18) Dasgupta, R., Chi, H., Shimizu, N., Buono, A. S. and Walker, D. (2013) 'Carbon
453 solution and partitioning between metallic and silicate melts in a shallow magma
454 ocean: Implications for the origin and distribution of terrestrial carbon', *Geochimica Et*
455 *Cosmochimica Acta*, 102, pp. 191-212.
- 456 19) Rose-Weston, L., Brenan, J. M., Fei, Y., Secco, R. A. and Frost, D. J. Effect of
457 pressure, temperature, and oxygen fugacity on the metal-silicate partitioning of Te, Se,
458 and S: Implications for earth differentiation, *Geochimica et Cosmochimica Acta*,
459 73(15), pp. 4598-4615 (2009).
- 460 20) Roskosz, M., Bouhifd, M. A., Jephcoat, A. P., Marty, B. and Mysen, B. O. Nitrogen
461 solubility in molten metal and silicate at high pressure and temperature, *Geochimica Et*
462 *Cosmochimica Acta*, 121, pp. 15-28 (2013).
- 463 21) Kadik, A., Koltashev, V., Kryukova, E., Plotnichenko, V., Tsekhonya, T. and
464 Kononkova, N. Solubility of nitrogen, carbon, and hydrogen in FeO–Na₂O–Al₂O₃–SiO₂
465 melt and liquid iron alloy: influence of oxygen fugacity, *Geochemistry International*,
466 53(10), pp. 849-868 (2015).

- 467 22) Li, Y.-F., Marty, B., Shcheka, S., Zimmermann, L. and Keppler, H. (2016) 'Nitrogen
468 isotope fractionation during terrestrial core-mantle separation'. *Geochemical
469 Perspective Letters*, 2 138-147
- 470 23) Dalou, C., Hirschmann, M. M., von der Handt, A., Mosenfelder, J. and Armstrong, L. S.
471 Nitrogen and carbon fractionation during core–mantle differentiation at shallow depth,
472 *Earth and Planetary Science Letters*, 458, pp. 141-151 (2017).
- 473 24) Speelmanns, I. M., Schmidt, M. W. and Liebske, C. Nitrogen solubility in core
474 materials, *Geophysical Research Letters*, 45(15), pp. 7434-7443 (2018).
- 475 25) Grewal, D. S., Dasgupta, R., Holmes, A. K., Costin, G., Li, Y. and Tsuno, K. The fate of
476 nitrogen during core-mantle separation on Earth, *Geochimica et Cosmochimica Acta*,
477 251, pp. 87-115 (2019).
- 478 26) Speelmanns, I. M., Schmidt, M. W. and Liebske, C. (2019) 'The almost lithophile
479 character of nitrogen during core formation', *Earth and Planetary Science Letters*, 510,
480 pp. 186-197.
- 481 27) Grewal, D. S., Dasgupta, R., Sun, C., Tsuno, K. and Costin, G. Delivery of carbon,
482 nitrogen, and sulfur to the silicate Earth by a giant impact, *Science advances*, 5(1), pp.
483 eaau3669 (2019).
- 484 28) Siebert, J., Corgne, A. and Ryerson, F. J. Systematics of metal–silicate partitioning for
485 many siderophile elements applied to Earth's core formation, *Geochimica et
486 Cosmochimica Acta*, 75(6), pp. 1451-1489 (2011).
- 487 29) Fischer, R. A., Nakajima, Y., Campbell, A. J., Frost, D. J., Harries, D., Langenhorst, F.,
488 Miyajima, N., Pollok, K. and Rubie, D. C. High pressure metal–silicate partitioning of
489 Ni, Co, V, Cr, Si, and O', *Geochimica et Cosmochimica Acta*, 167, pp. 177-194 (2015).
- 490 30) Suer, T.-A., Siebert, J., Remusat, L., Menguy, N. and Fiquet, G. A sulfur-poor
491 terrestrial core inferred from metal–silicate partitioning experiments, *Earth and
492 Planetary Science Letters*, 469, pp. 84-97 (2017).
- 493 31) Jackson, C. R., Bennett, N. R., Du, Z., Cottrell, E. and Fei, Y. Early episodes of high-
494 pressure core formation preserved in plume mantle, *Nature*, 553(7689), pp. 491
495 (2018).
- 496 32) Mahan, B., Siebert, J., Blanchard, I., Badro, J., Kubik, E., Sossi, P. and Moynier, F.
497 Investigating Earth's Formation History Through Copper and Sulfur Metal- Silicate
498 Partitioning During Core- Mantle Differentiation, *Journal of Geophysical Research:
499 Solid Earth*, 123(10), pp. 8349-8363 (2018).
- 500 33) Fischer, R. A., Cottrell, E., Hauri, E., Lee, K. K. and Le Voyer, M. (2020) 'The carbon
501 content of Earth and its core', *Proceedings of the National Academy of Sciences*,
502 117(16), pp. 8743-8749.
- 503 34) Ma, Z. Thermodynamic description for concentrated metallic solutions using interaction
504 parameters, *Metallurgical and Materials Transactions B*, 32(1), pp. 87-103 (2001).
- 505 35) Fiquet, G., Auzende, A. L., Siebert, J., Corgne, A., Bureau, H., Ozawa, H. and
506 Garbarino, G. Melting of Peridotite to 140 Gigapascals, *Science*, 329(5998), pp. 1516-
507 1518 (2010).
- 508 36) Badro, J., Brodholt, J. P., Piet, H., Siebert, J. and Ryerson, F. J. (2015) 'Core formation
509 and core composition from coupled geochemical and geophysical constraints',
510 *Proceedings of the National Academy of Sciences*, 112(40), pp. 12310-12314.
- 511 37) Iacono-Marziano, G., Morizet, Y., Le Trong, E. and Gaillard, F. (2012) 'New
512 experimental data and semi-empirical parameterization of H₂O–CO₂ solubility in mafic
513 melts', *Geochimica et Cosmochimica Acta*, 97, pp. 1-23.
- 514 38) Wallace, P. and Carmichael, I. S. Sulfur in basaltic magmas, *Geochimica et
515 Cosmochimica Acta*, 56, pp. 1863-1874 (1992).
- 516 39) Dreibus, G. and Palme, H. Cosmochemical constraints on the sulfur content in the
517 Earth's core, *Geochimica et Cosmochimica Acta*, 60(7), pp. 1125-1130 (1996).

- 518 40) Zhang, H., Hirschmann, M., Cottrell, E. and Withers, A. Effect of pressure on Fe³⁺/ΣFe
519 ratio in a mafic magma and consequences for magma ocean redox gradients,
520 *Geochimica et Cosmochimica Acta*, 204, pp. 83-103 (2017).
- 521 41) Armstrong, K., Frost, D. J., McCammon, C. A., Rubie, D. C. and Ballaran, T. B. Deep
522 magma ocean formation set the oxidation state of Earth's mantle, *Science*, 365(6456),
523 pp. 903-906 (2019).
- 524 42) Olson, P. and Sharp, Z. D. (2018) 'Hydrogen and helium ingassing during terrestrial
525 planet accretion', *Earth and Planetary Science Letters*, 498, pp. 418-426.
- 526 43) Fischer-Gödde, M. and Kleine, T. (2017) 'Ruthenium isotopic evidence for an inner
527 Solar System origin of the late veneer', *Nature*, 541(7638), pp. 525.
- 528 44) Wade, J. and Wood, B. (2005) 'Core formation and the oxidation state of the Earth',
529 *Earth and Planetary Science Letters*, 236(1), pp. 78-95.
- 530 45) Righter, K. and Chabot, N. L. Moderately and slightly siderophile element constraints
531 on the depth and extent of melting in early Mars, *Meteoritics & Planetary Science*,
532 46(2), pp. 157-176 (2011).
- 533 46) Edwards, C. S. and Ehlmann, B. L. (2015) 'Carbon sequestration on Mars'. *Geology*,
534 43(10), 863-866
- 535 47) Treiman, A. H. and Bullock, M. A. (2012) 'Mineral reaction buffering of Venus'
536 atmosphere: A thermochemical constraint and implications for Venus-like planets',
537 *Icarus*, 217(2), pp. 534-541.
- 538 48) Thibault, Y. and Walter, M. J. The influence of pressure and temperature on the metal-
539 silicate partition coefficients of nickel and cobalt in a model C1 chondrite and
540 implications for metal segregation in a deep magma ocean, *Geochimica et*
541 *Cosmochimica Acta*, 59(5), pp. 991-1002 (1995).
- 542 49) Tange, Y., Nishihara, Y. and Tsuchiya, T. Unified analyses for P- V- T equation of
543 state of MgO: A solution for pressure- scale problems in high P- T experiments,
544 *Journal of Geophysical Research: Solid Earth*, 114(B3) (2009).
- 545 50) O'Neill, H. S. C. and Eggins, S. M. The effect of melt composition on trace element
546 partitioning: an experimental investigation of the activity coefficients of FeO, NiO, CoO,
547 MoO₂ and MoO₃ in silicate melts, *Chemical Geology*, 186(1-2), pp. 151-181 (2002).
- 548 51) Japan Society for the Promotion of Science (JSPS) and the Nineteenth Committee on
549 Steelmaking. JSPS Steelmaking Data Sourcebook 273–297, Gordon and Breach
550 Science Publishers (1988).
- 551 52) Tsuno, K., Frost, D. J. and Rubie, D. C. The effects of nickel and sulphur on the core–
552 mantle partitioning of oxygen in Earth and Mars, *Physics of the Earth and Planetary*
553 *Interiors*, 185(1), pp. 1-12 (2011).
- 554 53) Badro, J., Aubert, J., Hirose, K., Nomura, R., Blanchard, I., Borensztajn, S. and
555 Siebert, J. Magnesium Partitioning Between Earth's Mantle and Core and its Potential
556 to Drive an Early Exsolution Geodynamo, *Geophysical Research Letters*, 45(24), pp.
557 13,240-13,248 (2018).
- 558

559 **Acknowledgments:** We acknowledge discussions with Ian Ocampo during a summer
560 internship at NMNH. We additionally acknowledge the support provided by C. Prescher, E.
561 Greenberg, and V. Prakapenka during the experiments conducted at GSECARS and in data
562 reduction. We thank Rob Wardell and Tim Rose for their support of the microscopy work
563 associated with this manuscript. We thank Tim McCoy for discussions regarding the model

564 results. CRMJ acknowledges support by NSF-EAR grant 1725315, Smithsonian GVP
565 fellowship, Carnegie Institute for Science (Geophysical Lab) Fellowship, and startup from
566 Tulane University. Portions of this work were performed at GeoSoilEnviroCARS (The
567 University of Chicago, Sector 13), the Advanced Photon Source, Argonne National Laboratory.
568 GeoSoilEnviroCARS is supported by the National Science Foundation—Earth Sciences (EAR-
569 1128799) and the Department of Energy—GeoSciences (DE-FG02-94ER14466). This research
570 used resources of the Advanced Photon Source, a US Department of Energy (DOE) Office of
571 Science User Facility operated for the DOE Office of Science by Argonne National Laboratory
572 under contract number DE-AC02-06CH11357.

573 **Author contributions:** All authors contributed to drafting of the manuscript and interpretation of
574 the data. CRMJ completed, prepared, and analyzed all experiments. CRMJ, ZD, and NRB
575 contributed to the design of LH-DAC experiments.

576 **Competing interests:** The authors declare no competing interests.

577
578 **Materials and Correspondence:** Correspondence and requests for materials should be
579 directed to Colin Jackson, cjackson2@tulane.edu

580
581 **Data and materials availability:** All data required to evaluate the conclusions of this paper are
582 presented in the paper and/or the Supplementary Information.

583
584
585
586
587
588
589
590
591
592
593

594

595

Figures

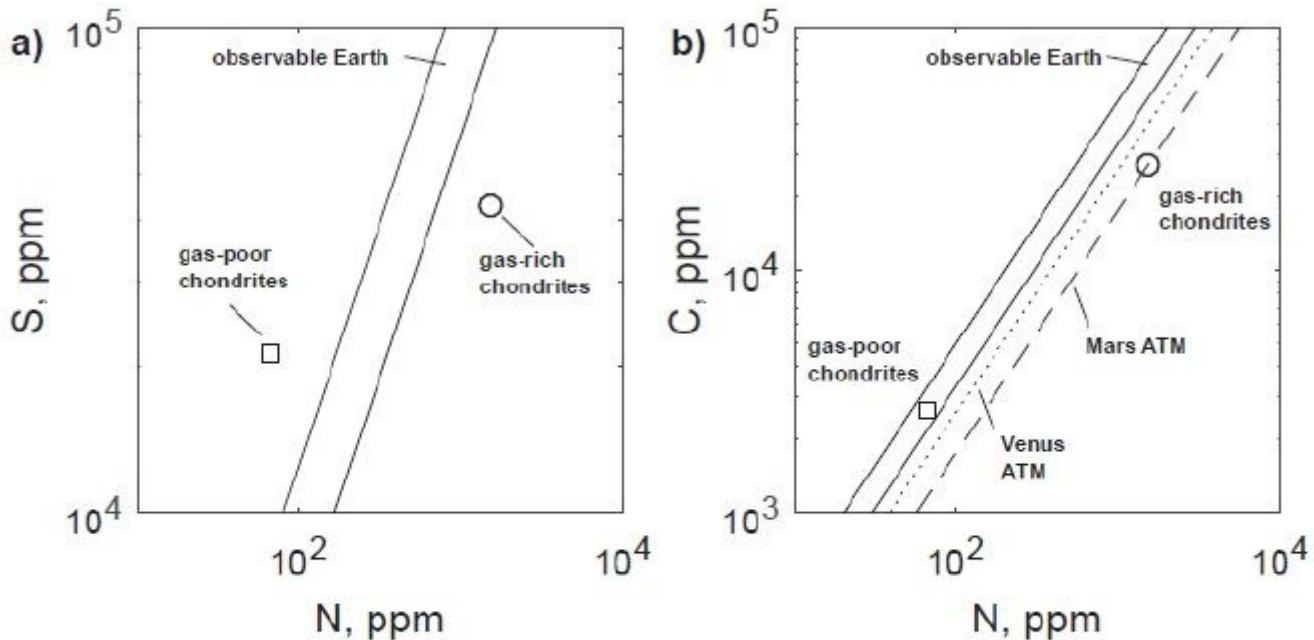


Figure 1: Observations of N-S-C ratios across terrestrial bodies. a) Sulfur and nitrogen concentrations of gas-rich (circle, average of CI and CM groups) and gas-poor chondrites (square, average of CO, CV, H, L, LL groups) compared to S/N ratio of the observable Earth ⁶. b) Carbon and nitrogen concentrations of gas-rich and gas-poor chondrites compared to C/N ratios of the observable Earth and the atmospheres of Mars ¹³ (dashed) and Venus ¹⁴ (dotted line). Chondrite data are from 7.

Figure 1

[See figure]

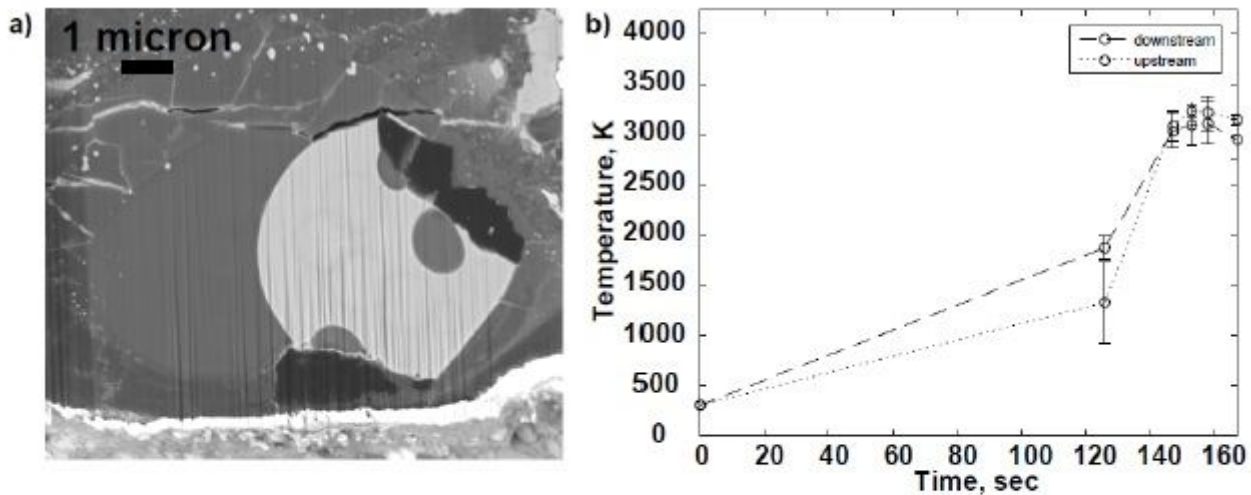


Figure 2: Representative figures in support of LH-DAC experiments. a) A backscattered image of heating spot 2. The light circle on right is the quenched alloy and darker regions with the alloy are C-rich. The darker region immediately to the left of the alloy is the quenched silicate. The heating spot is surrounded by ferroperricite. b) An example of a time-temperature path for a LH-DAC heating spot (heating spot 2). Both sides of the heating spot (upstream and downstream) have monitored throughout the heating duration. Error bars are the standard deviation of temperature measurement taken in rapid succession.

Figure 2

[See figure]

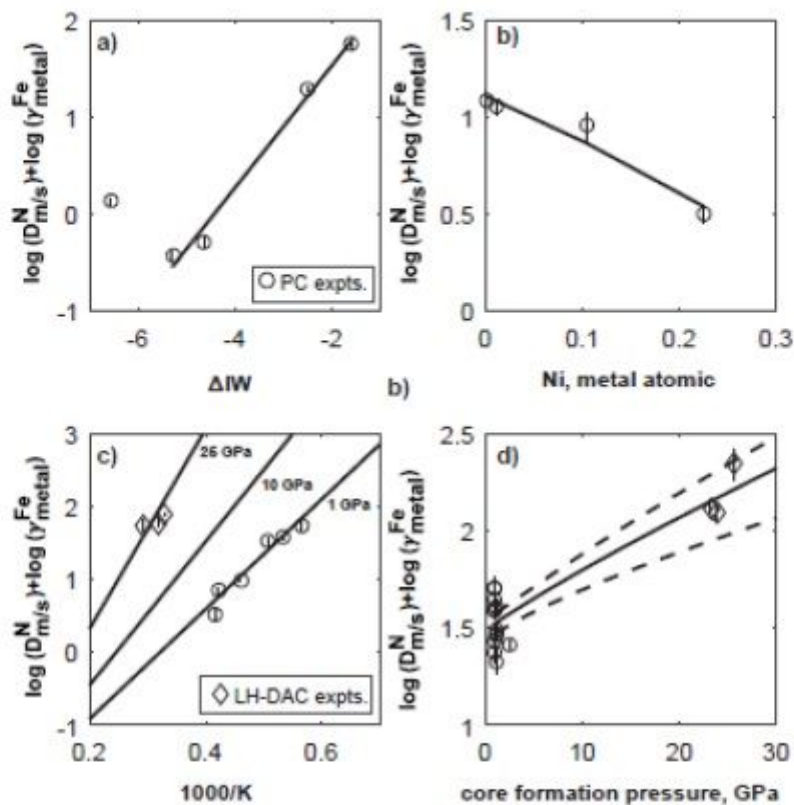


Figure 3: Major controls identified for nitrogen partitioning. a) More reducing conditions make nitrogen less siderophile between IW-1 and IW-5. The solid line is the least squares fit through data between IW-1 and IW-5. Below IW-5 there is preliminary evidence for a different redox sensitivity of N partitioning. b) Nickel makes nitrogen less siderophile. The solid line is the model fit to the Ni series experiments using the ϵ approach. c) Hotter conditions also make nitrogen less siderophile. Temperature series experiments were run at 0.95-1.05 GPa and 1773-2407 K. The solid line is the least squares fit of the temperature series data. Extrapolation of the temperature effect from ~ 1 GPa experiments to 3300 K (average core formation temperature) suggests N should be lithophile, but LH-DAC experiments completed near 3300 K and 25 GPa uniformly indicate moderately siderophile behavior. All data in c) have been corrected to IW-2 and a Ni-free composition using Eq. 1. d) Application of Eq. 1. to a core formation geotherm at IW-2 under C- and Ni-free conditions. Partitioning data are offset from the model by the difference between their measured value and the value predicted by Eq. 1. Nitrogen is increasingly siderophile with more extreme core formation *PT* conditions.

Figure 3

[See figure]

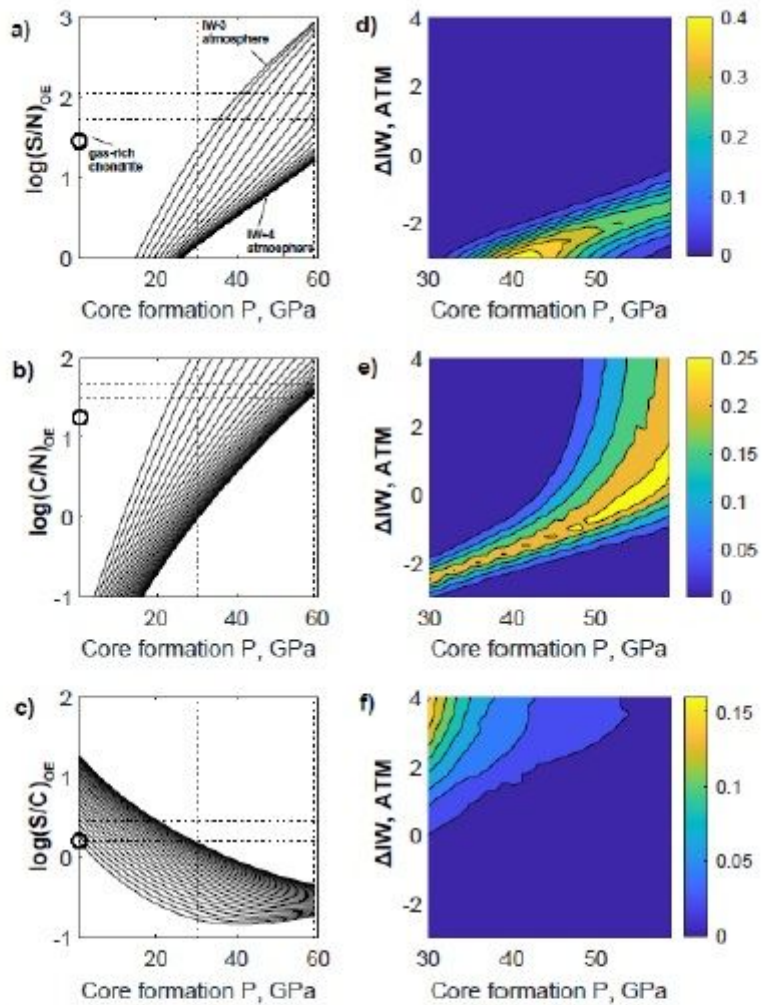


Figure 4: Equilibrium primordial differentiation model with bulk planet N-S-C ratios set by gas-rich chondrite. a-c) An example of a model iteration for a bulk Earth with a gas-rich N-S-C ratios. Observable Earth ratios are calculated for core formation occurring between 1-60 GPa and for magma ocean-atmosphere equilibrium between IW-3 to +4. Each line is a series of solutions with a constant atmospheric redox state. The redox spacing between lines is 0.25 log unit. The circles on the y-axes of a-c are the gas-rich chondrite ratios. d-f) Contour plots identifying atmospheric redox and core formation pressure conditions where observed volatile element ratios are satisfied. Equilibrium is complete between the primordial atmosphere, core, and a whole Earth magma ocean. The color bars denote the fractional success for the forward model for a given core formation pressure and atmospheric redox state.

Figure 4

[See figure]

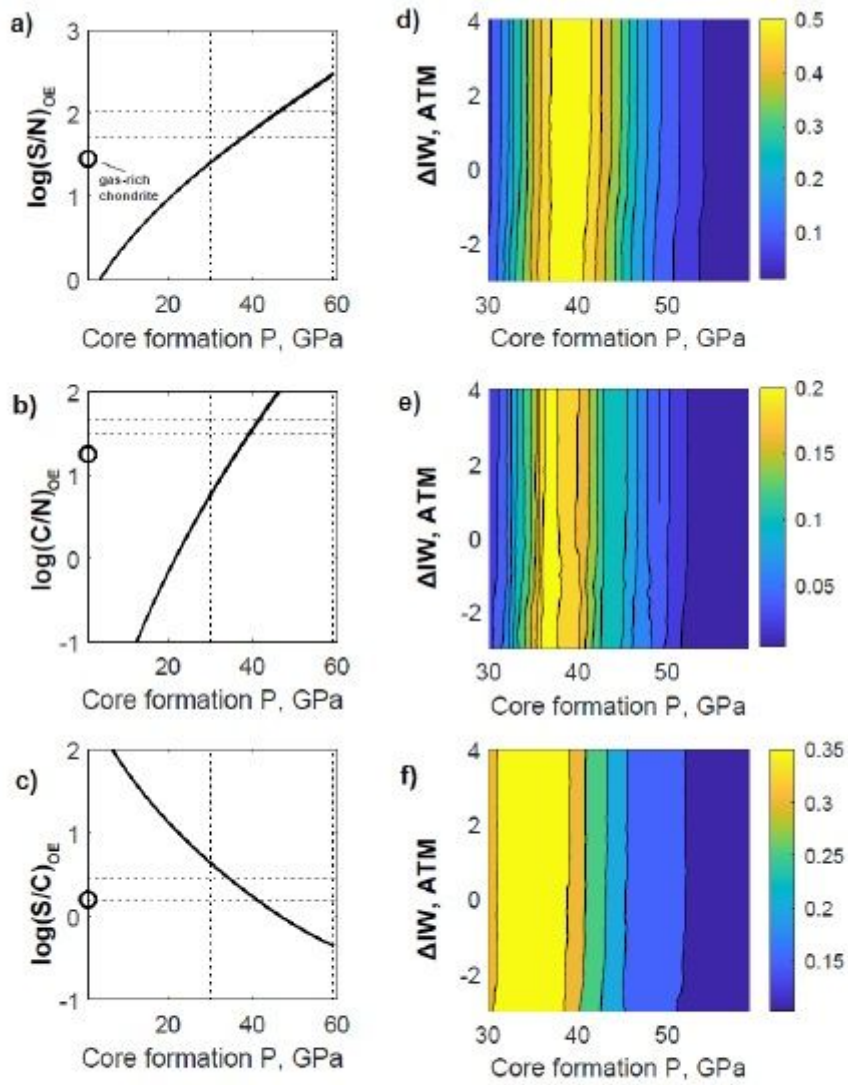


Figure 5: Disequilibrium primordial differentiation model with bulk planet N-S-C ratios set by gas-rich chondrite. Same as Figure 4, but with effective partial pressures of carbon and nitrogen 1000× higher in the magma ocean compared to the overlying atmosphere. Gas-rich chondrite ratios are given as squares on the y-axes of a-c.

Figure 5

[See figure]

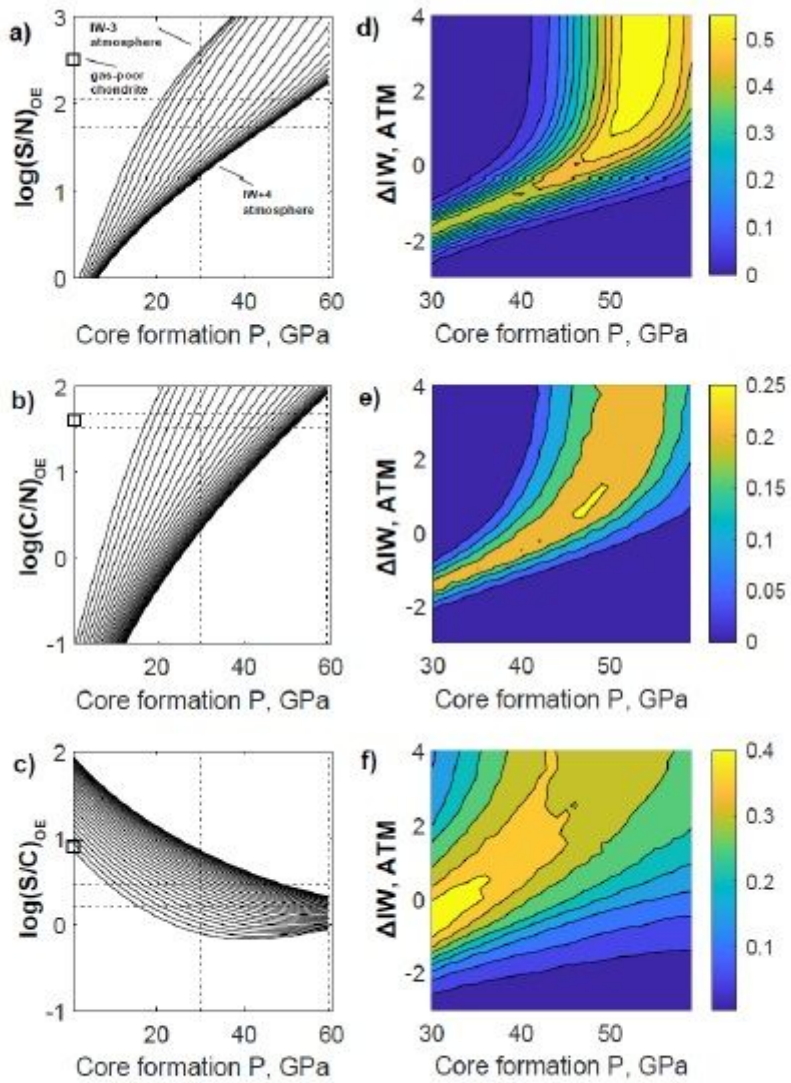


Figure 6: Equilibrium primordial differentiation model with bulk planet N-S-C ratios set by gas-poor chondrite. Same as Figure 4, but model assumes bulk planet with N-S-C ratios set by gas-poor chondrite. Gas-poor chondrite ratios are given as squares on the y-axes of a-c.

Figure 6

[See figure]

Supplementary Files

This is a list of supplementary files associated with this preprint. Click to download.

- [SupplementaryInformation.pdf](#)
- [Table1.xlsx](#)